IAEA nuclear fusion

PAPER • OPEN ACCESS

Particle fluxes and gross erosion at limiters in JET low-confinement mode plasmas measured with visible cameras

To cite this article: E. de la Cal *et al* 2025 *Nucl. Fusion* **65** 046021

OPEN ACCESS
IOP Publishing | International Atomic Energy Agency
Nuclear Fusion
Nucl. Fusion 65 (2025) 046021 (18pp) https://doi.org/10.1088/1741-4326/adbe8d

Particle fluxes and gross erosion at limiters in JET low-confinement mode plasmas measured with visible cameras

E. de la Cal[1,*], E.R. Solano[1], I. Balboa[2], S. Silburn[2], E. Pawelec[3], J. Romazanov[4], P. Carvalho[2], J. Karhunen[5], A. Tookey[2], S. Bakes[2], R. Chapman[2], J. Foster[2], A. Gonzalez[1], J. Maddock[2], J. Matthews[2], E. Pinto[2], I. Voldiner[1], L. Xiang[2], Y. Zayachuk[2] and JET Contributors[a]

[1] Laboratorio Nacional de Fusión,CIEMAT, Av. Complutense 40, E-28040 Madrid, Spain
[2] UKAEA (United Kingdom Atomic Energy Authority), Culham Campus, Abingdon, Oxfordshire OX14 3DB, United Kingdom of Great Britain and Northern Ireland
[3] University of Opole, Institute of Physics, Oleska 48, Opole, Poland
[4] Forschungszentrum Jülich GmbH, Institut für Energie- und Klimaforschung-Plasmaphysik, D-52425 Jülich, Germany
[5] Department of Applied Physics, Aalto University, 02150 Espoo, Finland

E-mail: e.delacal@ciemat.es

Received 17 May 2024, revised 24 January 2025
Accepted for publication 10 March 2025
Published 21 March 2025

Abstract

Deuterium (D) and beryllium (Be) fluxes are obtained in JET Low-confinement mode (L-mode) plasmas at the outer limiters of the first wall using calibrated visible cameras. They are inferred from the measured radiances using the spectroscopic S/XB method. From the fluxes, the effective gross erosion yield Y^{eff} of the limiter surface is estimated. After discussing the uncertainties in the proposed methodology, we show the dependence of the deduced particle fluxes and Y^{eff} of recent JET L-mode plasmas on: separatrix–limiter clearance, magnetic field and plasma current, neutral beam injection and ion cyclotron resonance heating power, average plasma density and majority ion mass, hydrogen (H), deuterium (D) and tritium (T). The results are in general accord with prior edge plasma L-mode understanding. Finally, the obtained Y^{eff} yields are discussed in view of updated SDTrim surface–particle interaction code calculations. The possible contribution of parasitic light due to reflections from the divertor is examined.

Keywords: first wall, L-mode, fluxes, spectroscopy, JET, cameras

(Some figures may appear in colour only in the online journal)

[a] See Maggi *et al* 2024 (https://doi.org/10.1088/1741-4326/ad3e16) for JET Contributors.
[*] Author to whom any correspondence should be addressed.

1. Introduction

In actual optimised tokamaks and stellarators, the main particle and heat fluxes diffusing outwards from the plasma are directed by the confining magnetic field towards the divertor. There the major plasma–surface interaction is controlled and decoupled to a large extent from the confined region (see e.g. [1, 2]). At the divertor, material erosion is reduced due to local cooling of the dense scrape off layer (SOL) plasma and radiation increased, allowing for smaller heat fluxes to the surfaces. Also, impurities can be effectively screened from the hot confined core plasma by the magnetic field, minimising its transport across the separatrix and the recycling fuel neutrals compressed so as to maximise their exhaust via pumping. This is the so-called semi or totally detached divertor operational scenario, which is envisaged for future burning reactors such as ITER or DEMO.

However, a considerable fraction of the particle (and heat) fluxes diffuse and convect across the magnetic field lines to the vessel first wall and limiters. Part of these fluxes is composed of Charge-Exchange (CX) neutrals, the other part, of ions and electrons escaping perpendicularly from the confining field. This last perpendicular transport, that competes with the parallel one towards the divertor, has a strongly turbulent nature (anomalous) and is especially strong at the plasma edge and SOL in L-mode plasmas (see e.g. [3–5]). The basic understanding of this is actually relatively limited, so that experimental quantification of particle and power fluxes are crucial to set-up empirical parametric scaling-laws of plasma magnitudes such as the particle and heat diffusion coefficients, which serve as input for plasma fluid and neutral transport codes. These are finally necessary for plasma–wall interaction and impurity transport codes such as ERO2.0 [6] or WallDYN-3D [7] to model plasma–surface interaction in next step fusion reactors, predict the surface erosion and re-deposition distribution and estimate T retention in co-deposits.

During the last years of JET operation, including hydrogen (H), tritium (T), helium (He) and deuterium–tritium (D–T) campaigns, a unique opportunity occurred to study and re-visit many key aspects for future devices such as ITER: reactor-relevant radiative scenarios with high confinement mode (H-mode) at high power (up to 35 MW), isotope effect on transport and plasma operation, L–H mode transitions, fusion-born α-particles, plasma–wall interaction, etc. (see an overview in [8]). Dedicated summaries of the main plasma–wall interaction results during the last campaigns can be found in [9, 10]. The data collected during the diverse operational scenarios that were run, now allowed us to extend and revise prior investigations. This is the case of the present work dedicated to first wall particle fluxes and Be surface erosion, a topic studied in the past mainly for ohmic D plasmas with contact point at the inner limiters viewed by a spectroscopy system [11–14]. A review on Be erosion can be found in [15]. A few years ago, visible cameras were used for the first time to reproduce the results to the same type of ohmic limiter plasmas, extend the studies to plasmas leaning at the outer limiters not accessible with other JET spectroscopic systems and explore the possibility to analyse plasmas with divertor configuration [16]. Also, taking advantage of the recent H, D and T campaigns, the isotope effect on the Be gross erosion was measured recently, confirming in JET the critical role of the hydrogenic ion mass on the Be sputtering yield [17], as predicted by particle–surface interaction codes and beam laboratory experiments.

The use of visible cameras applying spectroscopic analysis techniques such as the S/XB method, explained in the next section in more detail, is becoming a powerful tool in the last years. Their capacity to retrieve 2-dimensional information from large vessel areas is especially appropriate to monitor particle fluxes, which generally show significant toroidal and poloidal asymmetries. Here, the same cameras and methodology used in the past to study the D[6] and beryllium (Be) particle fluxes F and the gross erosion yield Y^{eff} in limiter plasmas, are applied to L-mode plasmas with divertor configuration. In the next section we describe briefly the camera system and the analysed plasmas. We explain then, how the particle fluxes are inferred from the measured emission intensities using the spectroscopic S/XB method. The approximations taken due to the scarce information on the SOL and edge plasma electron density n_{e} and temperature T_{e} are analysed and it is shown that the uncertainties are held within reasonable limits. Along the central part of the work, we explore the dependence of the fluxes F and Y^{eff} on different operational parameters: separatrix–limiter clearance, magnetic field B_{T} and plasma current I_{P}, neutral beam injection (NBI) and ion cyclotron resonance (ICR) heating power P_{NBI} and P_{ICR}, average plasma density $<n_{\mathrm{e}}>$ and plasma ion mass (hydrogen H, deuterium D and tritium T). Rather than making a detailed analysis on any specific point, the goal here is to obtain quantitative measurements of F and Y^{eff} and investigate their dependence on the different plasma parameters. Finally, we discuss the first wall erosion yield as obtained here in divertor configuration with previous equivalent studies in ohmic limiter plasmas and with the Be sputtering yields obtained from SDTrim surface–particle interaction code calculations [18]. The possible contribution of parasitic light reflections from the divertor is examined in a separate appendix.

2. Camera system and plasma description

In the present work, we use two of the five wide-angle visible cameras pertaining to a broadband wavelength viewing system operating in a range from the visible to the mid-infrared [19]. As part of a EUROfusion-JET diagnostic enhancement

[6] When saying deuterium or D in a general context, we refer also to H and T, but in the context of erosion, where the hydrogenic mass plays a significant role, the specific isotope denomination is used.

program for the recent D–T campaigns, the system has been successfully upgraded and later exploited at high neutron and Gamma radiation levels. For shielding purposes, the cameras were installed outside the JET biological protection wall. They receive the image from an endoscope installed at an equatorial port after being transported via a mirror based optical relay system along a path of about 40 m. The in-vessel optics images the JET vacuum chamber with two separate lines, a lower and an upper branch, each viewing one half of the machine. Both are then combined to form a full intermediate image after the port window. The cameras view is shown in figure 1, where (*a*) is a picture taken with internal vessel illumination and (*b*) is an image of an L-mode plasma image with the Be II filter with false colour scale. The frontier between the upper and lower image branches can be distinguished near the torus mid-plane. The region at the mid-plane of the outer limiter we study in the present work is marked with a rectangle. We have selected this region because there the whole plasma–limiter interaction region is visible and because the pixel resolution is sufficient to resolve the intensity distribution. It should be noted, that in the present work we will always consider the maximum intensities recorded by the cameras in this region, i.e. the estimated fluxes correspond to the utmost values.

The visible cameras used are the unfiltered visible 'high-speed or fast camera' and the 'spectroscopy camera' with filtering capacity. For the plasmas here analysed a narrow bandpass filter centred at the Be II line at 527.2 nm with 1 nm at full width at half maximum is employed. The camera has a 512 $\times$ 512, 16 μm pitch pixels electron multiplying CCD sensor with signal amplification capacity. The maximum recording speed is 80 frames per second (fps), but the exposure time can be reduced below the millisecond scale. The visible 'fast camera', with a CMOS sensor of 1024 $\times$ 1024, 17 μm pitch pixels, is able to record 3 $\times$ 10^3 fps at full frame and up to 2.5 $\times$ 10^5 fps at reduced active sensor size. The maximum recording time is limited to 2 GB so that the video length depends on both, the region of interest (ROI) size and the frame rate. The unfiltered visible measured light is strongly dominated by D_α-line emission as demonstrated in [20]. In fact, if a D_α-filter is put on the spectroscopy camera, the recorded images are equivalent to those of the unfiltered. Some applications of the two existing fast cameras in JET can be found in [21].

Both cameras were cross-calibrated against the absolute radiance measurements of the visible spectroscopy system monitoring the D_α and Be II lines looking to the divertor and to one inner Be limiter. The procedure is explained in detail in [16]. The final outcome of the calibration shows a very good agreement when comparing the absolute radiances of both lines when measured with the cameras and the spectroscopy system for different plasma conditions at the divertor and the inner limiter. The videos are visualized and analysed with the software framework JUVIL [22], which was specifically created to handle all the cameras of the JET viewing system.

The plasmas being investigated here were the L-mode phases of a series of different campaigns to study L–H transitions and carried out with varying plasma species content: H and D [23], T and DT [24] and HT mixtures [25]. All had the same plasma shape shown in figure 2, and (*a*) variety of B_T, I_P and electron density values were explored. In ICR heated plasmas and most NBI heated ones the power ramp rate was at most 1 MW s^{-1}. In T and D–T NBI heated plasmas 1 MW steps were taken every 1 s.

3. Plasma emission interpretation

A usual way to infer particle fluxes F[7] from limiters and the first wall is by spectroscopic means, analysing the line radiation emitted by the excited atoms entering the plasma and using the so-called S/XB coefficients [26]. These relate directly to the measured line integrated emission intensity of a characteristic atomic line expressed as radiance L with the particle flux F as:

$$F = 4\pi \mathrm{S/XB}L\,. \tag{1}$$

The S/XB coefficients are also called photon efficiencies or number of ionisation events per photon. They depend locally on T_e and n_e along the emission layer at the SOL plasma where most of the here analysed line radiation comes from. Commonly they are estimated using atomic collisional-radiative models and can be obtained from the ADAS database [27]. Unfortunately, there is scarce information on the T_e and n_e SOL profiles for the studied plasmas and approximations must be taken to estimate the S/XB values. However, as will be shown, thanks to their relatively small variations within our SOL T_e–n_e domain, this can be done accepting reasonable errors.

Figure 3 shows a schematic representation of the SOL plasma emission layer viewed by the cameras. D^+ plasma ions and D^0 CX neutrals impinging on the Be limiter surface and recycle on the surface as molecules and atoms. Since the D^+ and D^0 Recycling coefficient $R \approx 1$, the measurement of the D_2 and D neutrals re-entering the plasma is approximately equal to the incident flux. For the plasmas here analysed, with relatively short separatrix–limiter clearance (<5 cm), the main contribution of the D fluxes we observe at the outer limiter are D^+ ions. This can be affirmed because the D_α (and Be II) emission region there has a clearly peaked pattern near the outer mid-plane (OMP) where the separatrix–limiter clearance is smallest and where the plasma ions will preferentially impact. Light from recycled D^0 CX neutrals would in contrast show a rather homogenous distribution along the first wall. However, it should be remembered that when using the S/XB method, it is assumed that the emitting D atoms within the observing volume come from the corresponding associated area due to recycling, something that may not be always true, e.g. for energetic neutrals with a large ionization mean

[7] By fluxes F we refer in the present work to particles per unit time per unit area (s^{-1} cm^{-2}).

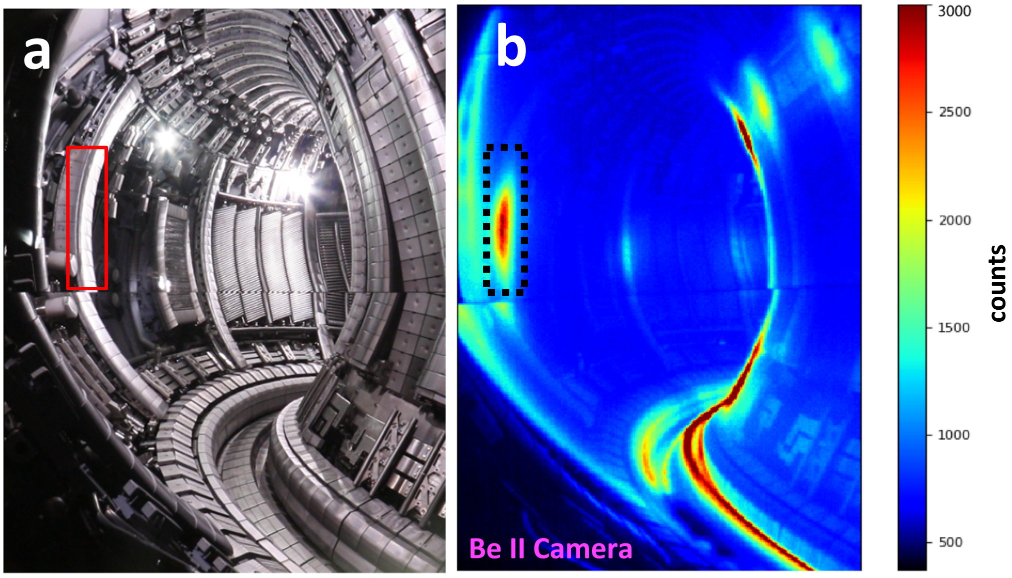

Figure 1. The cameras view inside the torus vessel: (*a*) is a picture taken with internal vessel illumination and (*b*) is an image of an L-mode plasma with the Be II filter. The region at the mid-plane of the outer limiter we analyse in the present work is marked with a rectangle.

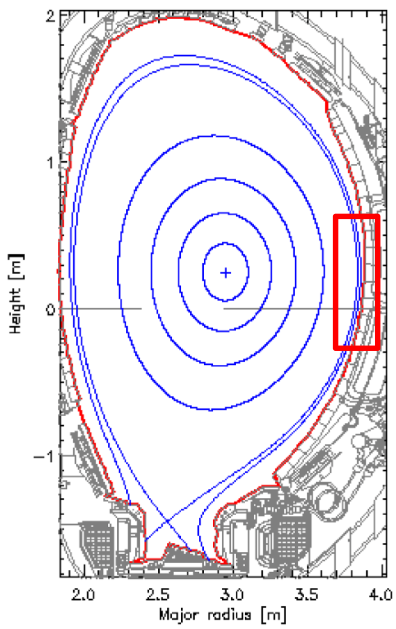

Figure 2. Plasma configuration of the analysed plasma and limiter observation region.

free path compared to the observation area dimensions. On the other side, the plasma flux onto the surface will release via sputtering (Be) impurity atoms from the material surface that are also measured in the present study. When entering into the plasma, the D and Be, apart from becoming ionized, get excited mainly via electron collisions and emit characteristic line radiation. Here we monitor with the cameras the D_α and Be II line at 527.2 nm lines, which converted to radiances, allow us to retrieve the corresponding particle fluxes. It should be outlined, that the generalised use of the Be II 527.2 nm line emitted by Be^+ ions in JET instead of a Be I line begun in earlier Y^{eff} studies to detect the BeD hydrides originated by chemical assisted physical sputtering (CAPS) without missing out the Be^+ fraction from dissociation reactions [12]. Choosing this line, it could be the case that a fraction of the sputtered neutral Be when entering the plasma and being ionized, is transported away from the observation volume or re-deposited before emitting the corresponding photons and therefore not counted for. We have however checked, that the estimated Be fluxes using a Be I line (at 457.4 nm) and its corresponding S/XB value are very similar to those obtained with the Be II 527.2 nm line for the same plasma. Therefore, this fraction of non-detected Be atoms should be small.

Returning to figure 3, where we have represented the radial profiles of n_e and T_e, which exponentially decay in the SOL plasma, and of a typical S/XB coefficient, which generally increases moderately with n_e and T_e for our typical SOL plasma conditions (see later). We also show illustratively the characteristic emission intensity profile I of the atomic line monitored by the camera, which peaks generally a few centimetres (say 2–5 cm) from the limiter surface. It is later converted to the radiometric unit radiance L using the respective calibration factor along the analysis process. The shape of I will mainly depend on the n_e and T_e profiles and of the speed of the atom entering into the plasma. Note that the intensity I measured by the camera integrates the emission along the viewing chord. On the other side, to get the particle fluxes from equation (1) we have to estimate discrete values for the corresponding S/XB coefficients weighted by the emission profile along the viewing chord. When doing this, assumptions must be made on the n_e and T_e profiles along the emission layer close to the surfaces. However, as will be shown later and as is generally the case, the S/XB coefficients do not vary much

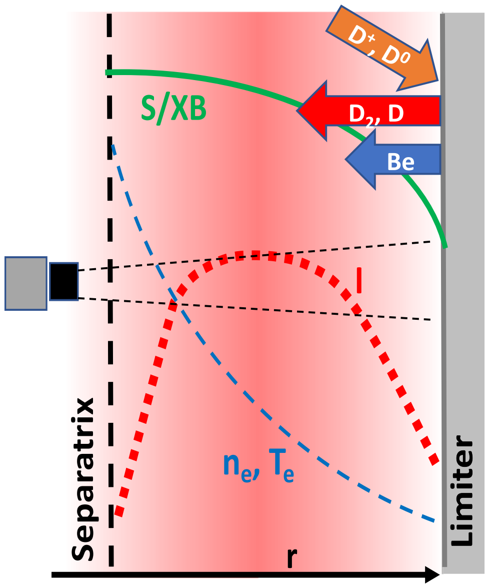

Figure 3. Schematic representation of the SOL plasma emission layer viewed by the cameras showing the radial n_e- and T_e-profiles (blue) together with those of S/XB (green) and the line emission intensity I (red).

for our SOL plasma conditions and reasonable approximations can be done.

The S/XB coefficients for D_α and the Be II retrieved from ADAS are plotted for 5 eV $< T_e <$ 200 eV in figure 4(a) for $n_e = 1 \times 10^{18}$ m^{-3} and 2×10^{19} m^{-3}. The ones for D_α do not consider the photons emitted by deuterium molecular reactions. In order to correct for this, a higher value by up to a factor of two must be foreseen [28, 29]. This contribution to the total D_α flux will depend mainly on the atomic/molecular physics near the emission layer, principally determined by the local n_e and T_e profiles there. Also, on the surface material and its temperature, which settle the molecular versus atomic fraction in the recycling process. A possibility to determine the molecular contribution of the S/XB is using neutral transport codes such as EIRENE, that considers all reactions that can lead to D_α line radiation as done in [30]. In this study, it was found that the dissociative excitation of D_2^+ can even dominate over the electron collision excitation of atomic D near the surface. In a recent study using EMC3-EIRENE [31], global S/XB values for the D_α line between 14 (in the far SOL plasma) and 34 (at divertor targets) are reported. On the other side, the way to experimentally estimate the molecular contribution is by measuring, besides the D_α line, also the molecular D_2 Fulcher band [28, 29]. Since a dedicated analysis on this is out of the scope here, relatively large errors must be foreseen when estimating the D fluxes (see later). However, when studying the flux variations as a function of plasma parameter, large relative deviations of the S/XB values are not to be expected. In other words, the error is mainly contained in the absolute value, not in its change.

In order to estimate the S/XB coefficients, we have firstly to delimit the n_e–T_e domain of the SOL for our plasmas, since most of the emission is expected to come from this region. In JET L-mode plasmas, depending on heating power and average density, we have from bibliography at the separatrix upstream plasma typically $n_e(a) \approx 0.5$–2×10^{19} m^{-3} and $T_e(a) \approx 30$–150 eV [32–35]. Further, the reported n_e and T_e near-SOL decay lengths λ_{ne} and λ_{Te} at the OMP are typically $\lambda \approx 2$–3 cm and increase towards the far-SOL up to double and more. The here analysed plasmas have a clearance or gap between separatrix and limiter of 45–50 mm near the OMP where the strongest plasma–surface interaction takes place. Thus, extrapolating from the separatrix with exponentially decaying functions the n_e and T_e can decrease down to about 1×10^{18} m^{-3} and 5 eV respectively at the limiter surface. Therefore, the whole SOL plasma n_e–T_e domain is covered in figure 4(a).

When choosing the S/XB value for a given line measurement, we have to estimate its line-integrated value weighted by the emission profile along the viewing chord. Unfortunately, there are no n_e nor T_e profiles available for the analysed plasmas and approximations must be taken. A reasonable approach is to take a value where we expect is the maximum of the emission intensity peak. It is typically located a few centimetres (about 2–5 cm) inside the material surface, from depending on the n_e- and T_e-SOL profiles. If we follow this criterion, we can limit the n_e–T_e range when estimating the line-integrated S/XB value. In figure 4(a), the shadowed regions mark this delimited parameter range where we expect is the emission maximum: 15 eV $< T_e <$ 100 eV and 5×10^{18} m^{-3} $< n_e < 2 \times 10^{19}$ m^{-3}. These limits are estimated from the separatrix $n_e(a)$ and $T_e(a)$ ranges given before and the SOL decay lengths λ. Following this approximation and looking to the graphs, in the present work we will use for all plasmas the intermediate or effective coefficients $(S/XB)_{BeII} = 45$ and $(S/XB)_{D\alpha} = 30$ to include the molecular contribution as explained before. They are marked with horizontal lines in the figure. The increase by about 50% for the D_α line to correct for the molecular contribution and spotted in figure 4(a) with an arrow was done to bring $(S/XB)_{D\alpha}$ to 30, which is the value recommended in [28, 29] near a limiter in ionizing plasma conditions (no recombination reactions).

With all this, the errors when fixing the line-integrated S/XB coefficients to constant values for all our analysed plasmas can reach up to ±25% for Be II and ±50% for D_α. To this we have to add other error sources, the most important being those coming from the S/XB ADAS calculations and those of the camera calibration factors. Concerning the calculated S/XB coefficients, we can say that depending on database, even within ADAS, one might find some differences, the origin of these being the specific CRM utilized and the atomic cross-sections used. For the widely used H_α (D_α) emission line there is, as far as we have seen in the different sources, no appreciable differences. For the Be II line at 527.2 nm we have found variations of about ±25% depending on the source. Concerning camera calibration factors, it must be noted that these were deduced making a cross-calibration against two spectroscopy systems, one looking to the divertor, the other to the inner guard limiters. The procedure is explained in [16].

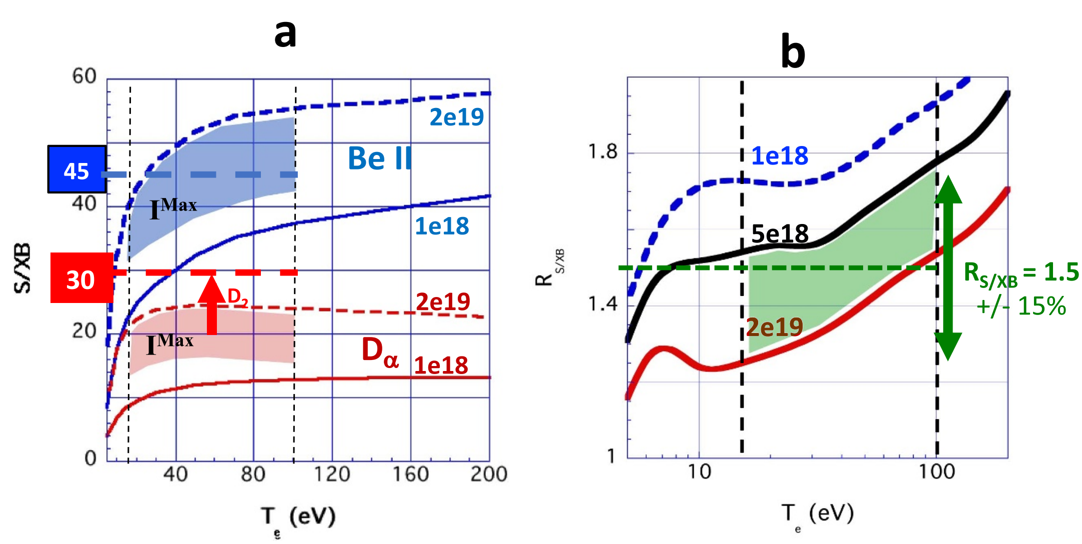

Figure 4. (*a*) S/XB coefficients for the D_α and the Be II at 527.2 nm retrieved from ADAS for different plasma densities. (*b*) $R_{S/XB}$ as obtained from the ratios of the D_α and the Be II S/XB coefficients.

Therefore, we have to add to the error in our cross-calibration process, the one existing inherently in these systems and the summation of both may give a relative uncertainty in the calibration factors of up to 50%. Summarizing, when extracting the particle fluxes from the camera intensities or counts, we have to accept an overall relative error of 100%. It should be however noted, that that these large uncertainties are common when quantifying spectroscopically plasma fluxes with the S/XB method. On the other side, most of these error sources are systematic meaning that when comparing relative values, a much smaller relative error should be expected. For example, if the fluxes are quantified and are seen to increase by a certain factor when making a parametric scan, then the expected uncertainty of the factor should be smaller than the value itself.

On the other side, the Be effective sputtering yield $Y^{eff}{}_{Be}$ (or simply Y^{eff}) is defined as:

$$Y^{eff}_{Be} \equiv \frac{F^{out}_{Be}}{F^{in}_{D}}, \quad (2)$$

where $F^{out}{}_{Be}$ is the Be out-flux sputtered from the surface by the bombarding plasma in-flux $F^{in}{}_{D}$[8]. The Be out-flux has two sputtering precursors from the plasma, the majority impinging D flux and the impurity flux, mainly Be in JET, that causes the so-called self-sputtering. On the other side, the major contribution to the Be erosion is physical sputtering, the other being CAPS, that produces the volatile molecule BeD. CAPS has been measured in JET to contribute up to 30% for D in the base operational limiter temperature of T < 300 °C and decreases as the surface temperature increases, vanishing for T > 500 °C [12]. For the here analysed plasmas the limiter surface temperature was below 300 °C (as measured by IR thermography) so that CAPS is expected to contribute significantly. In the present work we do not measure the BeD contribution from CAPS to the global erosion and we are not able to distinguish between both sputtering mechanisms. Nevertheless, we will later discuss its possible contribution.

From equations (1) and (2) we can retrieve $Y^{eff}{}_{Be}$ from the quotient of the Be II to D_α radiances as:

$$Y^{eff}_{Be} = \frac{(S/XB)_{BeII}\,L_{BeII}}{(S/XB)_{D\alpha}\,L_{D\alpha}} \approx R_{S/XB}\,\frac{L_{BeII}}{L_{D\alpha}}, \quad (3)$$

where $R_{S/XB}$ is defined as the S/XB ratio of the respective lines. Figure 4(*b*) shows $R_{S/XB}$ plotted in the range of 5–200 eV and three densities such as the whole n_e–T_e range expected in the SOL is covered. When calculating $R_{S/XB,}$ the ADAS S/XB of the D_α lines has been multiplied by 1.5 to include the molecular contribution. From the figure it can be seen that, since the S/XB coefficients of both lines have similar behaviours with n_e and T_e, their ratio $R_{S/XB,}$ has only small variations in this large n_e–T_e domain. Taking advantage of this, if a constant value of $R_{S/XB} = 1.5$ is taken, the maximum error in the whole plasma parameter range of the figure is about ±25%. The error is reduced to ±15% if we use the restricted range where we expect to be the line-integrated S/XB coefficients as explained before (blue shaded area in the figure).

4. Results

In the following section, the dependence of the particle fluxes F and the effective gross erosion yield Y^{eff} on different plasma parameters are studied: separatrix–limiter clearance, magnetic field B_T and plasma current I_P, NBI and ICR heating power P_{NBI} and P_{ICR}, average plasma density $<n_e>$ and plasma isotope mass (H, D and T). For all the selected discharges, the majority isotope has a minimum concentration of 90%, although generally it is above 95%. For each of the parametric scans, plasmas have been selected with similar values of the other parameters. For example, if we make a power scan,

[8] The subscript D stays here for deuterium, but may be replaced by H (hydrogen) or T (tritium).

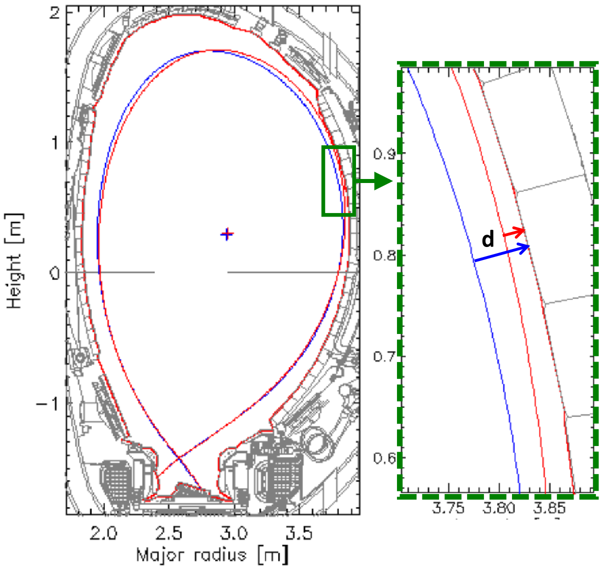

Figure 5. The separatrix at two time instants, $t = 14.5$ s (blue) and $t = 16$ s (red), of an L-mode plasma ($B_T = 2.4$ T, $I_P = 2$ MA) where the magnetic configuration was changed. The right frame is a zoom of the green rectangle and the arrows represents the clearance d.

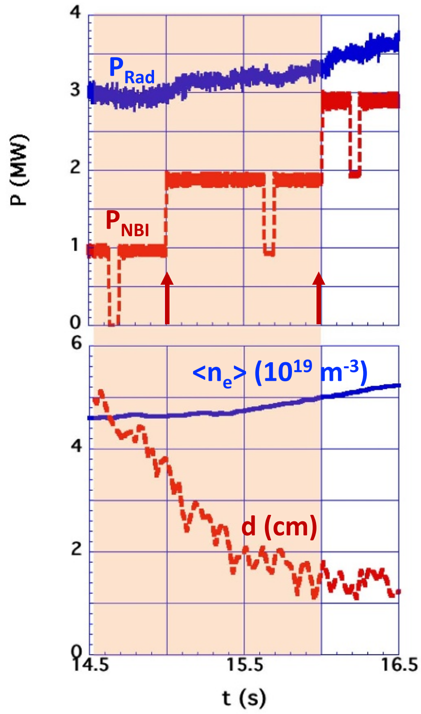

Figure 6. Time traces of the NBI injected power P_{NBI}, the total radiated power P_{Rad}, average electron density $<n_e>$ and clearance d.

we compare only plasmas with same or comparable B_T–I_P, $<n_e>$ and plasma isotope. Therefore, in some cases, the number of selected plasmas from the database is scarce. It should be mentioned, that an additional difficulty in the present work was to program in advance for each experiment the correct camera settings, as recording time, exposure time, amplification, field of view, etc. This was in the present work generally achieved thanks to the good coordination of the scientific team and the camera operators in the control room during each experimental session. Finally, we would like to note that in this broad study, rather than to make a detailed analysis on a specific parameter variation, the objective is to explore general trends and dependencies and let for the future more detailed analysis of individual specific topics.

4.1. Dependence on separatrix–limiter clearance

Figure 5 shows the separatrix at two time instants, $t = 14.5$ s (blue) and $t = 16$ s (red), of an L-mode plasma ($B_T = 2.4$ T, $I_P = 2$ MA) where the magnetic configuration was slightly changed. The clearance or gap d between the separatrix and the outer limiter marked with a red and blue arrow was reduced continuously during this time period from approximately 50 mm (blue) to 15 mm (red) at a height about 50 cm above the OMP. The time traces of the NBI injected power P_{NBI}, the total radiated power P_{Rad}, the average electron density $<n_e>$ and the clearance d are displayed in figure 6. The power P_{NBI} increases in 1 MW steps at the times marked with red arrows and $<n_e>$ raises slowly from 4.6×10^{19} m^{-3} to 5×10^{19} m^{-3} during the 1.5 s time interval when the clearance was reduced. Neither the rather small plasma density increase, nor that of P_{NBI}, should have a drastic influence on the fluxes compared to the effect of the clearance variation (see later). Figure 7 shows an image of an embedded video-clip from the Be II camera displaying the clearance reduction phase. As expected, there is a strong emission intensity increase when the separatrix approaches the outer limiter surface. The time evolution of the estimated maxima at the observation region of the T and Be particle fluxes within the green ROI are plotted in figure 8. The video recording time visible in the upper part of the clip corresponds to the time of figure 8 plus 40 s. The Be flux increases monotonically reaching a factor of 5 times larger compared to the initial state. The T flux, as estimated from the fast camera radiance, raises somewhat more moderately, ending with a value a factor of 3 higher than at the beginning. Using equation (3) the beryllium effective erosion yields are estimated to be: $Y^{eff} = 0.045$ for $d = 50$ mm and $Y^{eff} = 0.075$ for $d = 15$ mm. The observation that Y^{eff} increases when reducing d can be explained with the increase of the ion impact energy E_i at the limiter surface, something to be expected when reducing the gap to the separatrix. The strong plasma T ion flux $F > 10^{18}$ s^{-1} cm^{-2} onto the limiters for $d = 15$ mm is similar to the values we observed in the past for ohmic limiter plasmas with $B_T = 2.3$ T and $I_P = 1.9$ MA at the highest densities of 3.5×10^{19} m^{-3} [17].

In order to check quantitatively the T flux increase of figure 8, let us express F as a radially exponential decaying function along the SOL:

$$F(d) = F(0)\,e^{-d/\lambda_F}, \tag{4}$$

where d is the radial coordinate from the separatrix towards the limiter surface and λ_F the characteristic flux decay length,

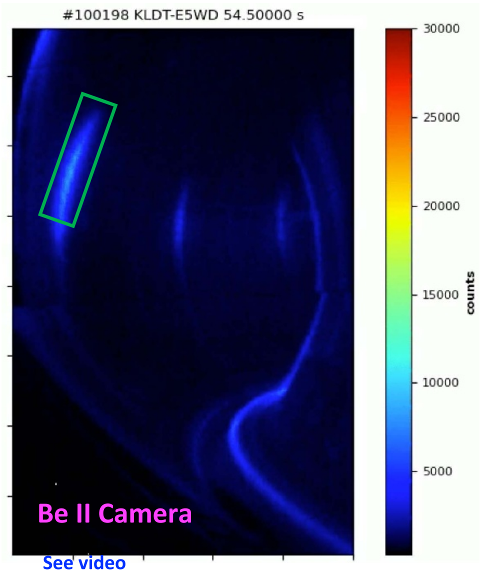

Figure 7. Video-clip of the Be II camera displaying the clearance reduction phase (the video is available in the online article).

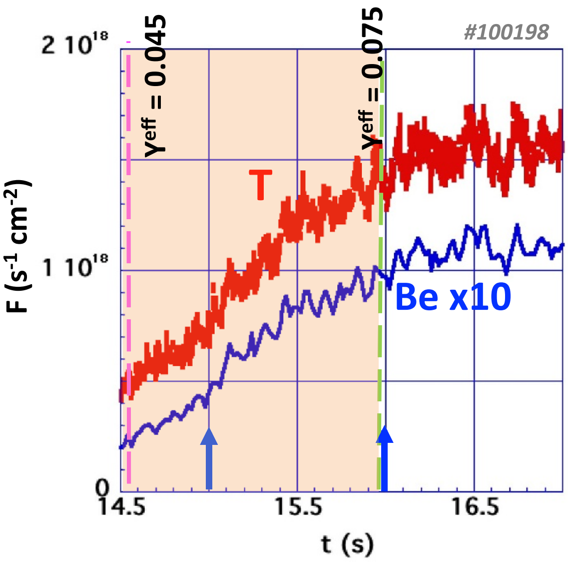

Figure 8. Time evolution of the estimated maxima of the T and Be particle fluxes.

which is related to the n_e and T_e SOL decay lengths as:

$$\lambda_F{}^{-1} = \lambda_{ne}{}^{-1} + (2\,\lambda_{Te})^{-1}. \quad (5)$$

From equation (4), introducing the measured fluxes at $d_1 = 50$ mm and $d_2 = 15$ mm we get a rough estimate of the flux decay length $\lambda_F = (d_1 - d_2)/\ln\,[F(d_2)/F(d_1)] \approx 30$ mm. This value is in good agreement with past JET L-mode SOL flux decay lengths deduced from the ion saturation current of a reciprocating probe [33] and is in general accordance with near SOL decay lengths $\lambda_{ne} \approx \lambda_{Te} \approx 20$–30 mm which increase at larger radii [35]. It must be noted, that this is a rather rough estimation of the flux decay length, since parameters as n_e and P vary during the measurement time period. The obtained value of λ_F however shows quantitative consistency with the expected one from prior work.

4.2. Dependence on magnetic field and plasma current

Figure 9 shows the images of the Be II and fast (D_α) cameras of three L-mode T plasmas (2 MW NBI, $<n_e> \approx 4 \times 10^{19}$ m^{-3}), with very similar magnetic configuration, but with different magnetic toroidal field B_T and plasma current I_P: (a) $B_T = 1.8$ T and $I_P = 1.8$ MA, (b) $B_T = 2.4$ T and $I_P = 2$ MA and (c) $B_T = 3$ T and $I_P = 2.5$ MA. For the fast camera images, only the limiter observation region is shown since to the intensity is strongly saturated at the divertor. As B_T and I_P increase, the Be II and the D_α (fast) emission decrease at the outer limiters (note that the scale is increased for frame a). Contrarily, at the divertor, the Be II intensity increases. The deduced particle fluxes at the limiter and divertor (only for Be) are plotted for the three plasmas in figure 10(*a*). We have assumed for the Be II line at the divertor the same S/XB values as at the limiter, although a smaller value is to be expected due to lower T_e there. The behaviour of the fluxes when increasing B_T and I_P can be explained with the expected reduction of the perpendicular transport with respect to the parallel one. In fact, when increasing these parameters, a shortening of the SOL density decay length λ_{ne} and a decrease of the density shoulder has been observed in JET L-mode plasmas [35]. The fit of the points in the figure was done with a power law $F\ \alpha\ B_T{}^a$, with $a \approx -1.5$ for the T fluxes and $a \approx -3$ for the Be fluxes. Note that this tentative fitting is just to show the tendency and much more points would be necessary to evaluate a trustful scaling law in a proper way. Moreover, an equivalent graph and fit can be made plotting F as a function of I_P. The quest whether which parameter influences on the fluxes cannot be answered, since for the analysed plasmas, B_T and I_P change together and it is not possible to separate their contributions. Finally, it should be also remembered that, as discussed in section 3, there is a large uncertainty of up to a factor of two when retrieving the fluxes, although the respective relative error between the points should be much smaller. This rule should be also generally true for the rest of the parametric studies here investigated.

In figure 10(*b*) are plotted the deduced Be effective erosion yields Y^{eff}, which shows a decrease by nearly a factor of 2 with increasing B_T and I_P. It points to a reduction of the ion impact energy E_i at the limiter surface, which would induce a sputtering yield decrement. This is consistent with observations in JET and ASDEX Upgrade L-mode plasmas, where the power decay length λ_q, proportional to λ_{Te}, was shown to decrease with increasing B_T as: $\lambda_q\ \alpha\ \lambda_{Te}\ \alpha\ B_T{}^{-0.8}$ [36]. Again, the here shown trend of Y^{eff} should be confirmed with more dedicated analysis in future.

4.3. Dependence on heating power

Another clear observation of the present study is that the type of plasma heating, ICRH compared to NBI, has a different impact on the particle fluxes and erosion yield. As a first example, we show in figure 11 for a D plasma ($B_T = 1.8$ T,

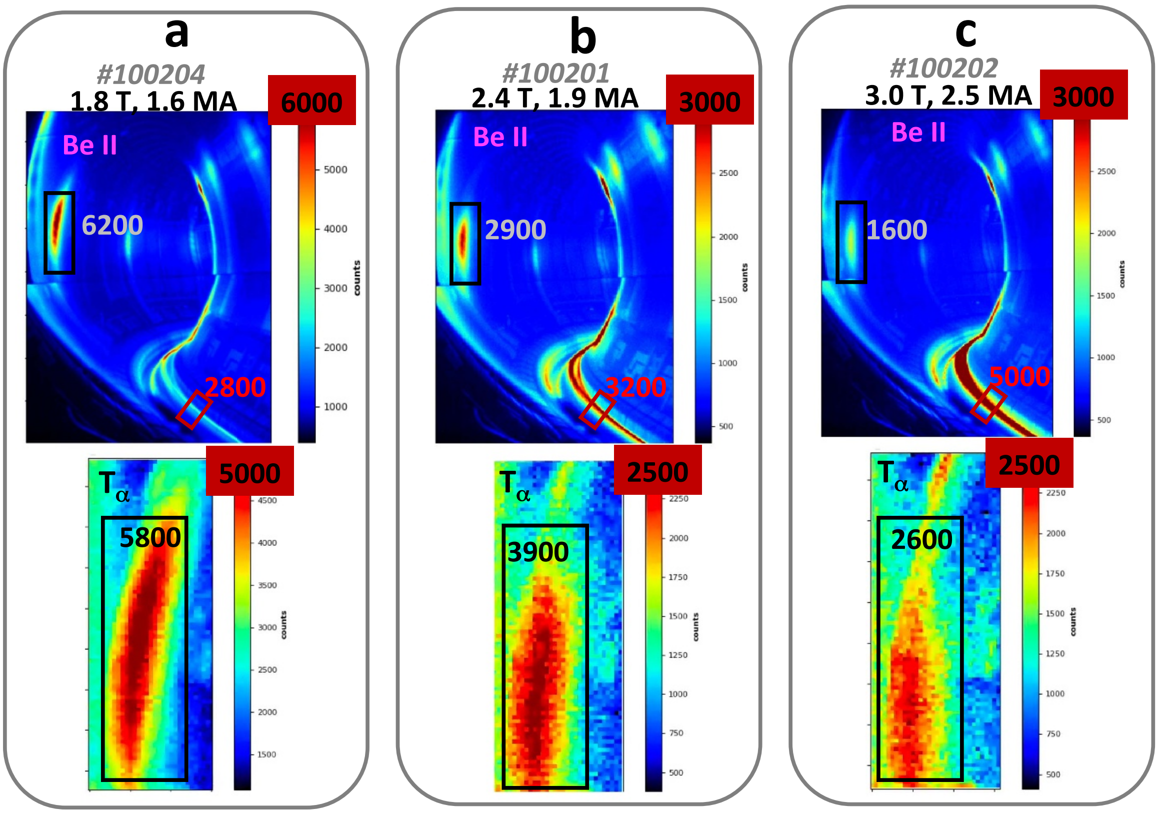

Figure 9. Images of the Be II and Fast (D_α) cameras of three T plasmas with very similar magnetic configuration, but with different magnetic toroidal field B_T and plasma current I_P (y-axis represents counts).

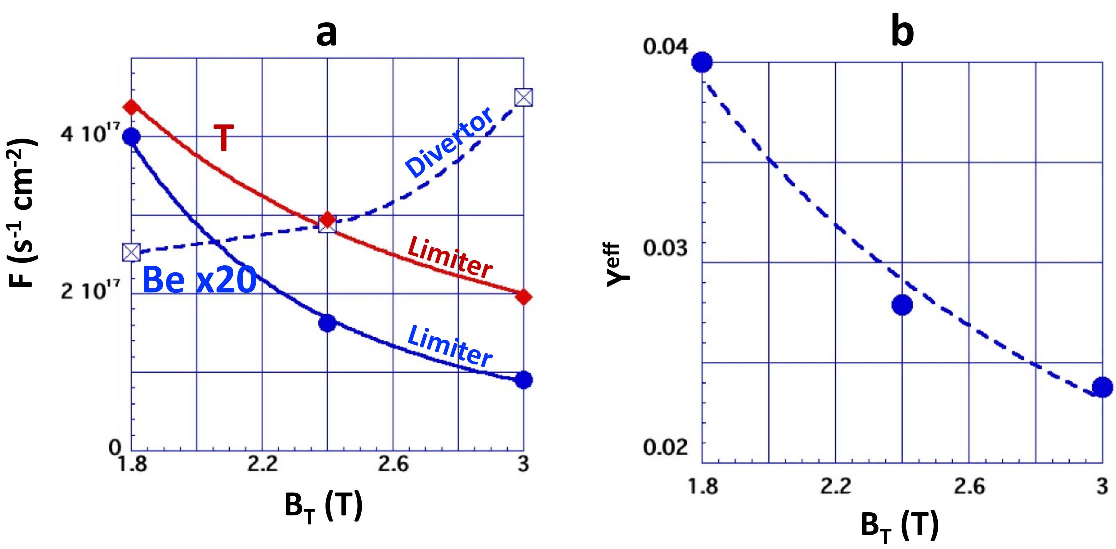

Figure 10. (*a*) Particle fluxes at the limiter and divertor (only for Be) for the three plasmas of figures 9 and (*b*) corresponding erosion yield Y^{eff}.

$I_P = 1.8$ MA) the time traces of injected power, P_{NBI} and P_{ICR}, the total radiated power P_{Rad}, the average density $<n_e>$ and the divertor D_α intensity. The plasma, firstly heated with NBI and transiting from L- to H-mode during the power increase, is later brought again from L- to H-mode during an ICRH power ramp. Before and after the first H-mode phase (blue shadowed fringe), the plasma has same $<n_e = 3\times10^{19}$ m^{-3} and 1 MW heating power, but at the beginning with NBI and later with ICRH. In figure 12 are plotted during the same time-interval the estimated particle fluxes of D and the Be as measured with the cameras at the outer limiter. The D fluxes are about 20% higher in the ICRH phase compared to the NBI phase. Those of Be increase by more than a factor of 2. The corresponding erosion yields are $Y^{\mathrm{eff}} \approx 0.025$ during NBI heating and

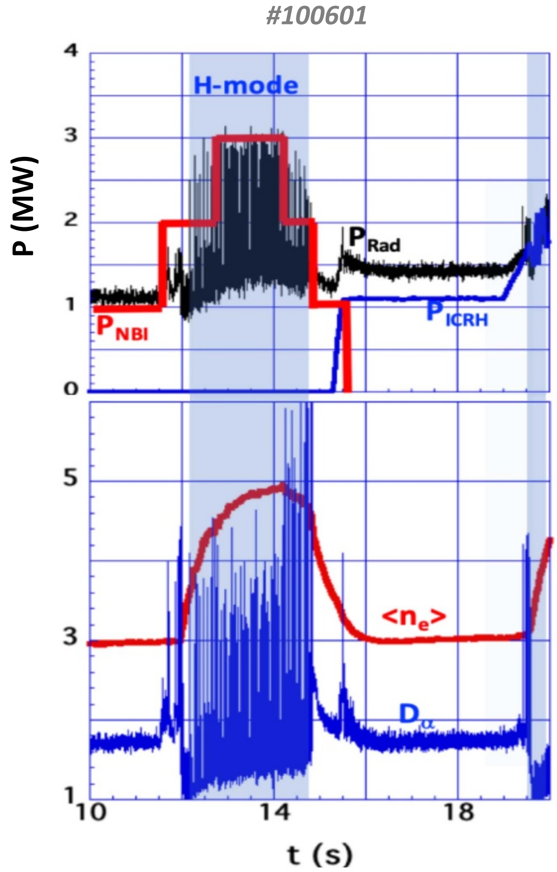

Figure 11. Time traces of injected power, P_{NBI} and $P_{\mathrm{ICR},}$ the total radiated power P_{Rad}, the average density $<n_e>$ and the divertor D_α intensity.

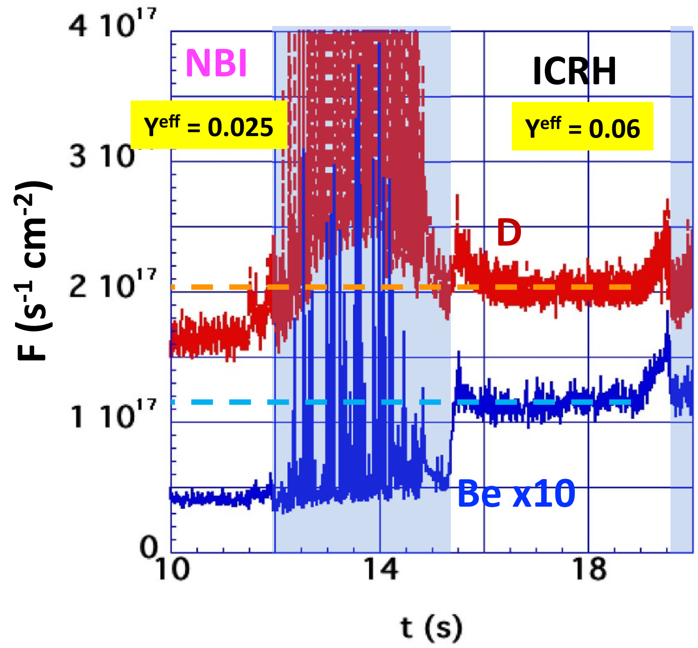

Figure 12. Particle fluxes of D and the Be at the outer limiter for the plasma of figure 11.

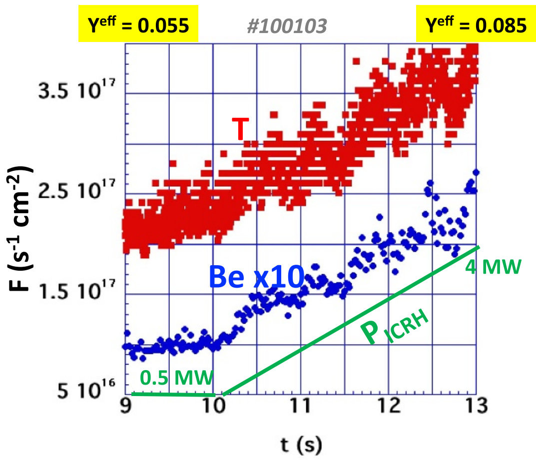

Figure 13. T and Be flux time traces for a T plasma where P_{ICR} was ramped from 0.5 MW to 4 MW (green line).

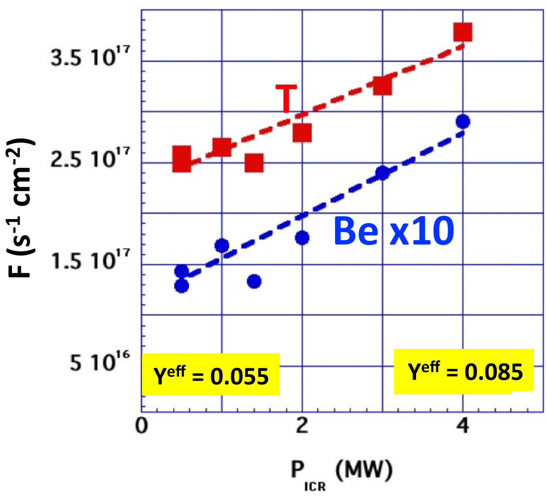

Figure 14. T and Be fluxes as a function of P_{ICR} for different T plasmas with similar $<n_e>$.

$Y^{eff} \approx 0.06$ during ICRH. The total radiation is about 30% larger during the RF heating phase indicating higher impurity content. This clearly much higher erosion yield in ICRH compared to NBI heated plasmas for similar power levels is systematically measured for all the plasmas analysed here. It is in accordance with generalised observations of enhanced metallic impurity production in ICRH heated plasmas, which is attributed to an increase of the ion energy onto the surfaces due to RF enhanced sheath potential, including in regions with unconnected field lines to the antennas (see review about influence of ICRH on SOL changes in [37]).

Moreover, there is a clear effect of the ICRH power level on the fluxes. Figure 13 shows the T and Be flux time traces for a T plasma ($B_T = 1.8$ T, $I_P = 1.8$ MA, $<n_e\geqslant = 3 \times 10^{19}$ m^{-3}) where P_{ICR} was ramped from 0.5 MW to 4 MW (green line) while the density stayed constant. The T fluxes increase during the power raise by a factor of 1.7 and those of Be by a factor of about 2.5. For 0.5 MW we get an erosion yield $Y^{eff} \approx 0.055$, which increases to $Y^{eff} \approx 0.085$ for 4 MW.

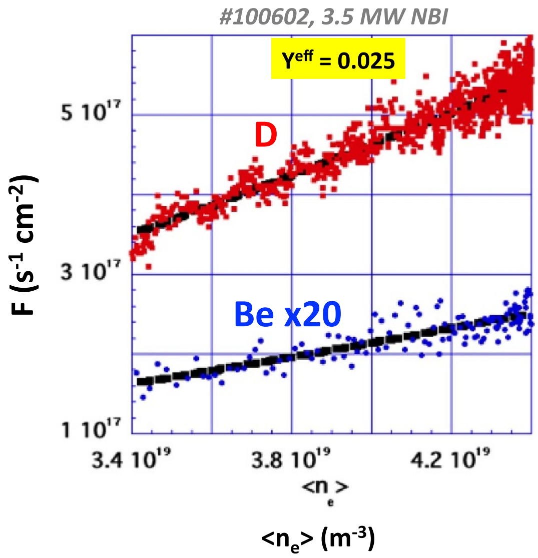

Figure 15. D and Be fluxes at the limiter as a function of $<n_e>$ during a plasma density ramp.

To confirm this trend, we have plotted the T and Be fluxes in figure 14 for a set of similar T plasmas but with different ICRH power levels ($B_T = 1.8$ T, $I_P = 1.8$ MA, $<n_e\geqslant = 3 \times 10^{19}$ m^{-3}). A similar increment of the fluxes with P_{ICR} is observed. Also, the estimated erosion yields Y^{eff} show a similar increase with ICRH power. Contrarily, for NBI heated plasmas we do not observe any clear increase of the fluxes with the power, at least within the relatively small range we have investigated. As an example of this, we just refer to the NBI power scan shown in figures 6 and 8. It can be seen that at the moments at which two power steps of 1 MW are done (see arrows) any sensible increase in the fluxes occur.

4.4. Dependence on average plasma density $<n_e>$

The D and Be particle fluxes at the limiter near the OMP are plotted in figure 15 as a function of $<n_e>$ during a plasma density ramp ($B_T = 3$ T, $I_P = 2.5$ MA, $P_{NBI} = 3.5$ MW). Both fluxes steadily increase by about 60% during the $<n_e>$ ramp-up of about +30%. The effective erosion yield $Y^{eff} \approx 0.03$ stays constant within this density range. Fitting the fluxes to a power law (dashed black lines) we get for both, D and Be: $F \ \alpha <n_e>^{1.7}$. A stronger $<n_e>$ dependence was found for a set of T ICR heated plasmas with same power level $P_{ICR} = 2$ MW ($B_T = 1.8$ T, $I_P = 1.8$ MA) as can be seen in figure 16. The fit of the data to power laws give: $F_D \ \alpha <n_e>^3$ and $F_{Be} \ \alpha <n_e>^{2.5}$. The deduced yield is $Y^{eff} \approx 0.075$, a factor of 3 higher than the former NBI case.

Generally speaking, we can say that for the L-mode plasmas analysed here, the increase of the particle fluxes with $<n_e>$ is clearly larger than for limiter plasmas studied in the past, which showed a nearly proportional dependence with

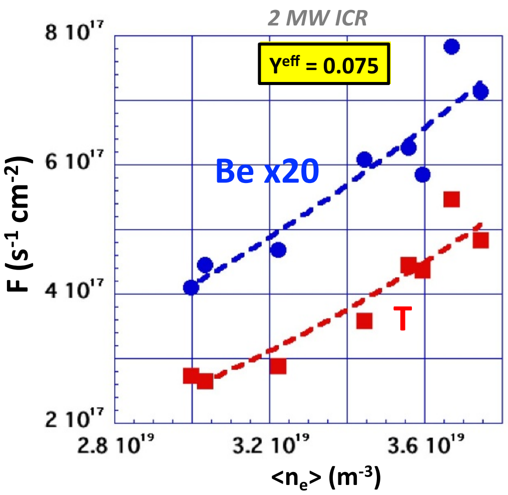

Figure 16. Same as figure 15 for a set of T ICR heated plasmas ($P_{ICR} = 2$ MW).

average plasma density [16]. This observation of enhanced fluxes is accordance with the characteristic enhanced perpendicular (turbulent) transport across the SOL in L-mode plasmas and with the development of the density shoulder when increasing $<n_e>$ (see e.g. [3–5 and 35]).

4.5. Dependence on plasma isotope mass

Figure 17 shows two images from the Be II filtered camera of (*a*) a hydrogen (98% H) and (*b*) a tritium dominated (90% T, 10% H) plasma. Both discharges belong to the same experimental session and had same plasma parameters ($B_T = 1.8$ T, $I_P = 1.7$ MA, $<n_e> = 3 \times 10^{19}$ m^{-3} and $P_{ICR} = 4$ MW). The camera settings were the same in both. At the outer limiter observation region, the H_α (T_α) emission at this moment were similar in both, indicating similar H (T) fluxes. However, the Be II emission intensity is about three times stronger for the T discharge as can be deduced from the images. This indicates a much higher erosion yield for T. The total radiated power was a factor of 2 higher in the T plasma, indicating a higher impurity content. A systematic comparison of similar H and T ICRH heated plasmas ($B_T = 1.8$ T, $I_P = 1.7$ MA, $<n_e> \approx 3 \times 10^{19}$ m^{-3}) of the isotope effect on the erosion yield is shown figure 18, where Y^{eff} is plotted as a function of P_{ICR}. As in the section 4.3, we see a clear increase of Y^{eff} with the applied power for T, but not for H, something that is not understood for the moment. Important is the clear isotope mass effect: T has an erosion yield a factor of about 2 higher than H. A similar result was recently observed in JET ohmic limiter plasmas [17]. As will be discussed later, this isotope effect is in good agreement with ion beam laboratory experiments and surface–particle interaction code calculations [38, 39].

5. Discussion

Let us compare the here obtained Be effective erosion yields Y^{eff} in diverted L-mode plasmas with those obtained recently for H, D and T ohmic limiter plasmas analysed with the same methodology [17] and also with the physical sputtering yields Y^{Phys} calculated with the surface–particle interaction code SDTrim. In order to compare both yields, we have to subtract from our Y^{eff} measurements the contribution of CAPS, which is not considered in the Y^{Phys} SDTrim calculations.

Figure 19 shows Y^{eff} as a function of $<n_e>$ for the past analysed ohmic limiter plasmas for H, D and T. As in the present work for L-mode plasmas, the measured Y^{eff} showed a clear increase with the isotope mass, the increments being in good agreement with ion beam laboratory experiments and surface–particle interaction code calculations [38, 39]. Additionally, the general trend is that, as already observed in the past [11–14], the erosion yield decreases with increasing plasma density due to the diminution of T_e and thereby E_i at the limiter surfaces decreases. The inflexion region at medium densities is an artefact, since as in the present work, a constant value was fixed for the $R_{S/XB}$ ratio rather than a slowly varying n_e and T_e function. For these ohmic limiter plasmas, the contribution of CAPS on Y^{eff} was extracted thanks to the use of a visible spectrometer that monitored the production of molecular beryllium hydride (BeH). The estimated fraction of CAPS was around 30% for D [12], 25% for T and 50% for H [17, 40]. The relative importance of CAPS on the total yield increases with decreasing ion mass, because CAPS is observed to stay constant independently of the hydrogenic mass, whereas the global Y^{eff}, the sum of physical sputtering and CAPS, decreases. This means that the observed isotope effect on Y^{eff} is only linked to the well-known ion mass effect on the physical sputtering yield.

Table 1 summarises the measured Y^{eff} ranges for H, D and T without CAPS for ohmic limiter plasmas from the past and for the here analysed L-mode plasmas with $d = 4.5$ cm, $B_T = 1.8$ T and $I_P = 1.7$ MA. For the L-mode plasmas a similar CAPS contribution as in limiter plasmas was subtracted. This assumption may underestimate this fraction, since prior experimental studies in PISCES and molecular dynamics (MD) modelling indicate that the relative contribution of CAPS increases when decreasing the impact energy [41, 42].

In figure 20 are plotted the Be physical sputtering yields Y^{Phys} as a function of ion energy E_i from updated SDTrim calculations for the three isotopes H, D and T assuming 45° incidence angle [43]. The graphs are plotted only for $E_i < 100$ eV to better show the energy range to be discussed. The general trend of the yields is following: $Y^{Phys} = 0$ below a certain threshold energy, then increases with E_i up to a maximum near 100 eV, stays quite flat in the range 100 eV $< E_i <$ 500 eV (not shown) and finally decreases moderately for higher energies. On the graph, we have overlaid the Y^{eff} ranges of table 1 without CAPS, i.e. only including physical sputtering (coloured ellipses)

For ohmic limiter plasmas there is good agreement with the calculated curves for the three isotopes near the calculated Y^{Phys} maximum values. The lower ion energy limit, to match onto the curves the Y^{eff} measured ranges corresponds to $E_i \approx 75$ eV. Assuming $T_e \approx T_i$ and $E_i \approx 5\ T_e$ [12], this would mean that we have at the limiter surface for the higher densities (lower Y^{eff}) $T_e \approx 15$ eV. This is in good agreement

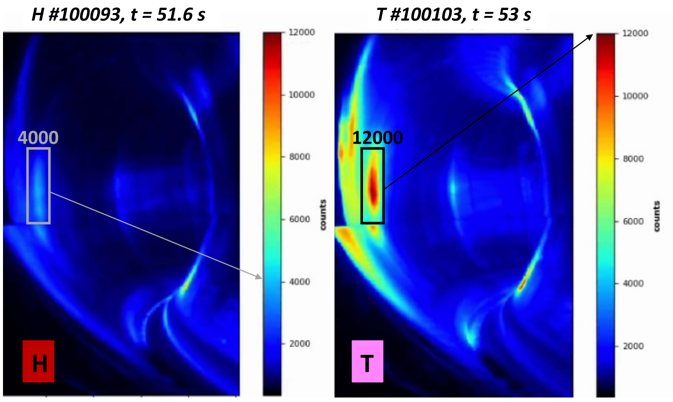

Figure 17. Be II filtered images of (*a*) a hydrogen (H) and (*b*) a tritium dominated (90% T, 10% H) plasma.

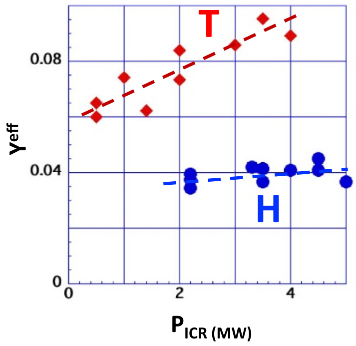

Figure 18. Y^{eff} as a function of P_{ICR} for different T and H plasmas.

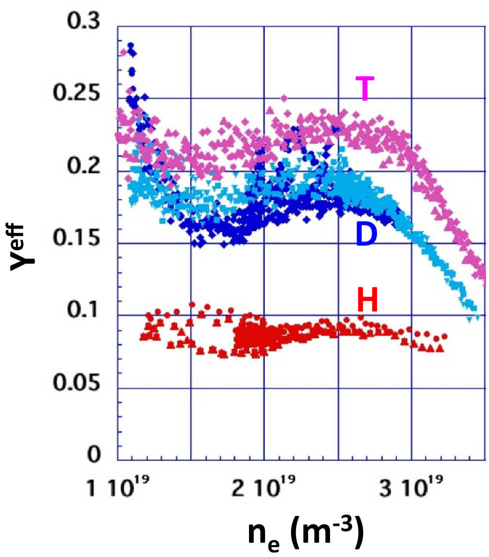

Figure 19. Y^{eff} as a function of $<n_e>$ for H, D and T in ohmic limiter plasmas.

Table 1. Effective erosion yields Y^{eff} without CAPS for ohmic limiter and L-mode plasmas.

	H	D	T
Y^{eff} limiter	$4\text{–}5 \times 10^{-2}$	$1\text{–}1.5 \times 10^{-1}$	$1.5\text{–}2 \times 10^{-1}$
Y^{eff} L-mode	$2\text{–}2.5 \times 10^{-2}$ (ICR)	2×10^{-2} (NBI)	$4\text{–}7 \times 10^{-2}$ (ICR)

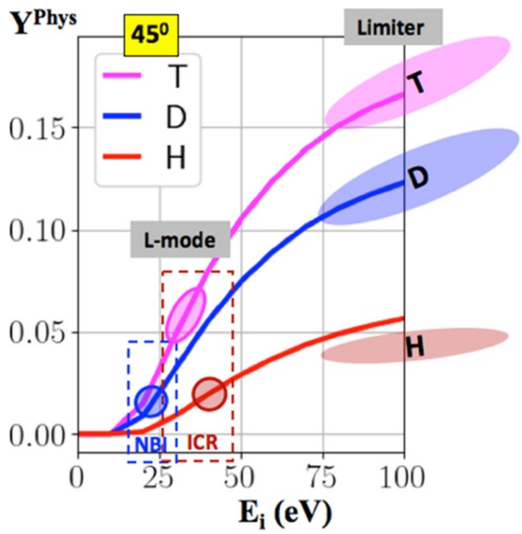

Figure 20. Physical sputtering yields Y^{Phys} as a function of ion energy from updated SDTrim calculations for the three isotopes H, D and T assuming 45° incidence angle. The ellipses mark the measured Y^{eff} yields without CAPS for ohmic limiter and diverted L-mode plasmas.

with probe measurements for high density ohmic limiter plasmas, where $T_e \approx 20$ eV were measured [32, 44]. As the plasma density decreases, T_e increases up to about 100 eV, meaning that E_i reaches up to 500 eV for lowest $<n_e>$ in ohmic limiter plasmas.

Fort the L-mode plasmas, the Y^{eff} ranges here obtained when plotted on the SDTrim curves, correspond for the ICRH plasmas to impact energies of around $E_i \approx 25$–50 eV. This would correspond to $T_e \approx 5$–10 eV at the limiter surface. For NBI plasmas somewhat lower values are to be expected since minor Y^{eff} were measured. This is also in accordance with probe measurements of $T_e \approx 10$ eV and lower in JET L-mode plasmas at about 50 mm from the separatrix [32, 33].

It should be clarified when looking to figure 20, that unfortunately we have no measurements of E_i (nor T_e) at the limiter surface. Also, that the estimated erosion yields marked on the SDTrim curves have relatively large errors. The idea here is just to try to show on one side, that the corresponding measured values between the different isotopes, where the relative error should be much smaller, are consistent with those of modelling. On the other side we try to display, that the energy ranges that match the yields of the curves are also quite reasonable in view of the expected values for limiter and L-mode plasmas.

Summarising, the comparison of sputtering yields from measurements and calculations shows a consistent picture with the expected T_e in ohmic limiter and L-mode plasmas and the corresponding impact energies. The dependence with the ion mass is also in good accordance for the three isotopes. As a final remark, it should be remembered that the gross erosion yields given in table 1 correspond to the L-mode plasmas with small clearance ($d < 5$ cm) and low $B_T = 1.8$ T and $I_P = 1.8$ MA. These are quite unfavourable parameters from the point of view of wall erosion, since as shown in section 4, the yield Y^{eff} decreases when increasing d and B_T (I_P). In ITER for example, $d \geqslant 8$ and $B_T \geqslant 4$ T, much lower yields and plasma fluxes F_D than those here reported are to be expected. It should be also remembered, that the here quantified particle fluxes (per unit area) correspond to peak values at discrete poloidal limiters. One should foresee much lower values in case of a toroidal limiter as in ITER, since the global fluxes will be distributed over a much larger area.

6. Summary and future work

In the present work we show that visible cameras with a wide-angle view are a useful tool to study and quantify particle fluxes inside the vessel of a magnetic confinement fusion device. They allow here to monitor simultaneously the divertor and a large part of the vessel, including inner, outer and upper First wall and limiters. Here we analyse the D fluxes to the outer limiters and those of the sputtered Be during L-mode plasmas. They are inferred from two absolutely calibrated cameras using the spectroscopic S/XB method. From the fluxes, the effective gross erosion yield of Be (Y^{eff}) is then deduced. In a separate appendix it is shown, that for the here analysed plasmas, with relatively small separatrix–limiter clearance (<5 cm), the contribution of parasitic light reflections from the divertor is small. We have explored the dependence of the fluxes and Y^{eff} on different plasma parameters. Even if we do not go in detail to any of the broad aspects here inspected, following trends have been observed:

- As envisaged, particle fluxes strongly increase when reducing the separatrix–limiter distance. A 35 mm shortening of the clearance raise the D fluxes by a factor of about 3 and those of Be by about a factor of 6. This means that Y^{eff} grows when reducing this distance, an indication that the ion energy increases at the limiter surface. The estimated near SOL particle flux decay length $\lambda_F \approx 30$ mm is in accordance with typical near-SOL decay lengths λ measured in JET L-mode plasmas (section 4.1).
- When increasing B_T and I_P, the fluxes to the limiter clearly decrease, in consonance with a reduction of the perpendicular versus the parallel particle transport. The limiters receive nearly 3 times lower plasma fluxes with $B_T = 3$ T and $I_P = 2.5$ MA compared to those with $B_T = 1.8$ T and $I_P = 1.8$ MA. We also observe a Y^{eff} decrease when incrementing B_T and I_P, indicating a reduction of the ion impact energy E_i. This is in accordance with prior studies in JET L-mode plasmas where the SOL power flux decay length λ_q and thereby of λ_T and of T_e at the limiter surface was seen to decrease with increasing B_T (section 4.2 and [36]).
- ICR heated plasmas induce somewhat higher D fluxes and much higher Be fluxes compared to NBI plasmas for same power levels. We systematically observe for plasmas with same parameters (P, B_T, I_P and $<n_e>$) much higher Y^{eff} values by a factor of 2–3 when heating with ICR compared to NBI. Additionally, the fluxes and the effective erosion yield Y^{eff} increase considerably with the ICR heating power level. The enhanced erosion and impurity production induced by

the ICR heating in the SOL plasma has been observed in many machines (section 4.3 and [37]).

- Both, the D and Be fluxes, increase much stronger than linearly with the average plasma density. Assuming a power law $F \alpha <n_e>^a$, we got for an NBI plasma $a \approx 1.7$ and for a set of ICRH plasmas $a \approx 2.5$. This is in line with prior observations of enhanced perpendicular turbulent transport across the SOL in L-mode plasmas when increasing $<n_e>$ and with the broadening of the density shoulder (section 4.4, [4, 5, 35]).
- Y^{eff} increases with the plasma isotope ion mass: for T we get yields a factor of about 2 higher compared to H. This isotope effect is in good agreement with prior ion beam laboratory experiments, surface–particle interaction code calculations and recent studies in ohmic limiter plasmas (section 4.5 [17, 38, 39],).
- The comparison of measured Y^{eff} with physical sputtering yields from SDTrimp calculations shows an overall consistent picture with the expected impact energies for ohmic limiter and L-mode plasmas and with the plasma isotope ion mass. This shows the importance of these kind of experimental studies to validate surface–particle interaction and erosion simulation codes (section 5).

Concerning future work, a similar study is being carried out for high-power ITER-baseline H-mode plasmas of last JET campaigns including D–T mixtures. The effect of impurity (Neon, Nitrogen) seeding and of ELM size is investigated. Despite the much higher heating power of up to 35 MW in these plasmas, we will show that it is difficult to retrieve the particle fluxes for the inter-ELM period. This is because the separatrix–limiter clearance and the operation B_T–I_P was set larger compared to the plasmas here analysed. As shown in the present study, these parameters strongly reduce the ion particle fluxes and increase the relative contribution of CX neutrals. Therefore, we observe less highlighted emission at the limiters compared to other wall areas. Additionally, the contribution of D_α parasitic divertor reflections also increases, something that complicates the emission interpretation at the First wall. In view of this, the analysis of these plasmas is a challenge. The quantification of stray light would be very desirable. The methodology would be similar as the one proposed in [45–47], briefly described in the appendix below. The idea is to firstly produce synthetic D_α camera images using the CHERAB code with inputs from the analysed plasmas using fluid and neutral transport codes (SOLPS and EDGE2D-EIRENE). Then estimate the reflections with a ray-tracing code using the surface reflection properties already characterized in JET for most first wall tile components. Finally, compare the synthetic images, including the reflections with those from the real camera. This experiment-modelling validation study would be of great interest for the development of analysis and simulation tools for future devices such as ITER.

Acknowledgments

This work has been carried out within the framework of the EUROfusion Consortium, funded by the European Union via the Euratom Research and Training Programme (Grant Agreement No 101052200—EUROfusion). Views and opinions expressed are however those of the author(s) only and do not necessarily reflect those of the European Union or the European Commission. Neither the European Union nor the European Commission can be held responsible for them.

This research was also supported in part by the Grants FIS2017-85252-R and PID2021-127727OB-I00, funded by MCIN/AEI/ 10.13039/501100011033 and by 'ERDF A way of making Europe'.

Appendix. Light reflections at the limiters from the divertor

Due to the much stronger D_α radiation at the divertor compared to that at other regions such as the limiters, surface light reflection can lead to incorrect interpretation of the emission. Dealing with reflections or stray light in fusion devices is a complex subject-matter and a software framework called CHERAB was developed for modelling spectroscopic diagnostics with a ray-tracing package for different European tokamaks including JET [45, 46]. It is configured to model the scrape-off layer line emission from plasma fluid and neutral transport simulations. The bidirectional reflectance distribution function, that characterizes the surface reflection properties, was obtained through a series of calibration photos of in-vessel point lights for most JET first wall tile components. Using high fidelity plasma fluid simulations for obtaining the plasma D_α emission distribution, the technique was able to simulate plasma images of a JET divertor camera so as to extract the reflection effects when comparing them to the real recorded images. More recently a new method for estimating the erosion of Be in ITER has been proposed. It uses ray tracing-aided tomography to reconstruct the three-dimensional profile of Be visible-light emissivity from synthetic images of filtered cameras and other diagnostics [47]. The Be emissivity inside the vessel is retrieved from the Be^0 and Be^+ distribution from ERO2.0 simulations. The contribution of surface light reflections on the different spectroscopic diagnostics can then be estimated and subtracted.

In the present work it is out of the scope to apply such methodologies to estimate the effect of parasitic light. Here we will just show, that for the here analysed plasmas, with relatively short separatrix–limiter clearance (<5 mm) at the OMP and thereby relatively high plasma particle fluxes, surface reflections should contribute only weakly to the D_α emission there. We will do this with empirical observations, e.g. analysing the local spatial emission pattern very similar to that of the Be II. Another argument to show the weak contribution of reflections, is the lack of temporal correlation of the D_α emission

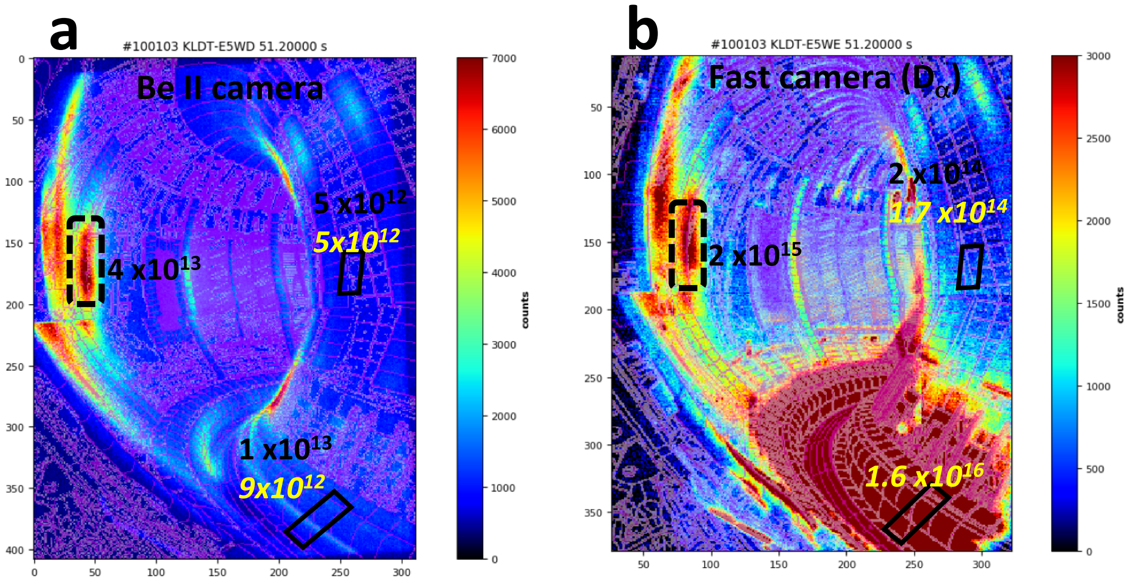

Figure A1. Images of a typical L-mode plasma taken at the same time with (*a*) the Be II filtered and (*b*) the unfiltered fast camera (D_α emission).

time traces at the divertor and the measurement region at the outer limiter.

Figure A1 shows the images of a typical L-mode plasma taken at the same time with (*a*) the Be II filtered and (*b*) the unfiltered fast camera dominated by D_α emission. The measured radiances (in photons s^{-1} sr^{-1} cm^{-2}) at three ROIs, divertor, outer limiter and inner wall, are marked on the figures: in black as estimated with the calibrated cameras and in yellow with the divertor and inner wall spectroscopy system (not available at the outer limiter). The values of both are in very good agreement. Looking to the Be II image we see that the radiance at the outer limiter mid-plane is larger than at the divertor. For the here studied plasmas, where the separatrix–limiter clearance at the OMP $\leqslant$ 5 cm, we always have a smaller or similar Be II intensity at the divertor. We can therefore conclude, that for the Be II emission at the outer limiter observation region, reflections coming from other vessel regions are not an issue. This is not the case for the D_α emission, where emission from the divertor is always much stronger than at the outer limiter as can be seen in image (*b*). In fact, due to the limited dynamic range of the fast camera, the settings used to analyse the outer limiter emission brings the level at the divertor to saturation so that we have to use the spectroscopy system to get the D_α radiances there. Looking to the wall, we see that the radiance distribution is quite homogeneous being typically a factor of 100 lower than at the divertor. This points to reflections from the divertor and/or emission from recycled CX neutrals. Contrarily, the light coming from the outer limiters is peaked at OMP, where the clearance is smallest. Moreover, the spatial distribution is very similar to that of the Be II emission as will be shown with more detail below and the intensity is about a factor ten higher than at the walls. It should be noted, that after ([44], see figure 9(*a*)), the divertor D_α stray light reflection distribution should be similar for all the Be vessel components of the wall and the limiters. This is not the case here with the localized peaked emission regions at the outer limiters clearly highlighted with respect to the rest of the wall.

Let us analyse the spatial limiter emission distribution in more detail. In a past publication ([16], section 5), it was shown with a high-speed video (50 μs exposure time), how filamentary coherent structures convect radially towards the limiters in an L- to H-mode dithering plasma. Here, since the fast camera exposure time was set a factor of about ten higher, time integration hinders the recognition of the individual filaments. However, we can observe in the consecutive frames randomly appearing inhomogeneous emission structures in the fast and the Be II cameras, result of the time-integration of the individual events (see embedded videos figure A2(*a*)). When comparing two frames of both cameras corresponding to the same recording time, a high correlation of the patterns can be recognized, as shown in figure A2(*b*). This observation is unlikely to be explained by reflections or parasitic light, but much more likely by real physical emission inhomogeneities produced by the SOL plasma turbulence.

A further argument indicating that for the here analysed plasmas, the D_α emission at the outer limiters near the OMP is not dominated by divertor reflections is the lack of temporal correlation of the emission intensities at both regions. Figure A3(*a*) shows an image taken with the fast camera at the moment where an ICRH power ramp brings the plasma from L- to M-mode shortly before entering in H-mode. We have marked on the image four ROIs: Divertor, Limiter and also Wall 1 and 2 at the outer lower and inner midplane first wall regions respectively. In the upper frame of figure A3(*b*) is plotted the D_α radiance time evolution averaged over the inner divertor (black) as measured by a fast spectroscopy system (fast camera is saturated). Strong D_α oscillations appear in phase with an MHD mode with a frequency of about 50 Hz. Also shown is the D_α radiance multiplied by 100 measured by another spectrometer with a horizontal view at the inner wall at the region corresponding to the ROI named Wall 1 (red). We

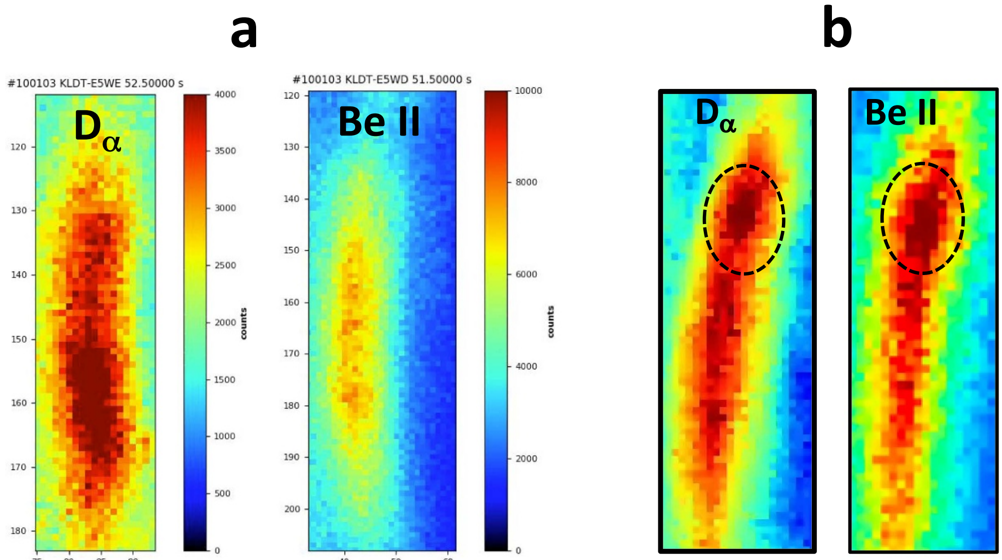

See video See video

Figure A2. (*a*) Video-clips of D_α and Be II (the videos are available in the online article) emission at the outer limiter. (*b*) Comparison of two selected frames of the video-clips.

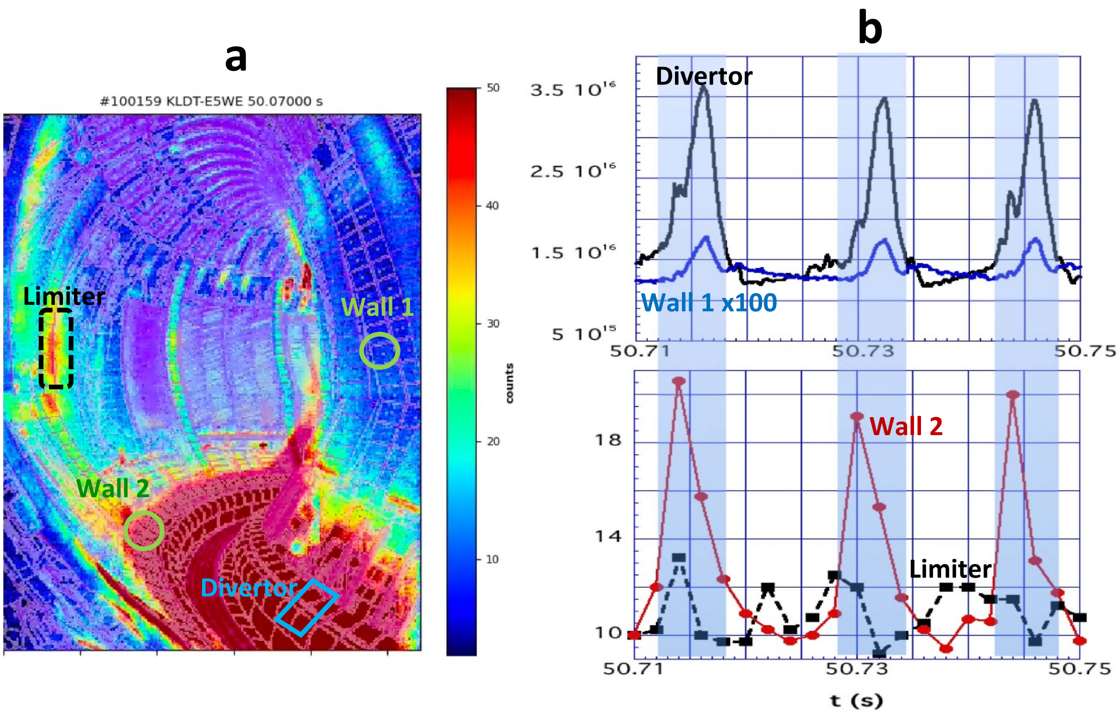

Figure A3. (*a*) Fast camera image with selected ROIs at the divertor, walls and limiter. (*b*) Upper frame: D_α radiances at divertor (black) and inner wall (blue) as measured by two spectroscopy systems. Lower frame: intensities measured by the fast camera at the limiter (black squares) and at the wall near the divertor (red circles).

see the same modulation as at the divertor and in phase. Due to the similarities in the waveform, one can suspect that the emission from the inner wall near the mid-plane may have a significant fraction of reflected light from the divertor. In the lower frame are plotted with a lower temporal resolution the intensities measured by the fast camera at the outer limiter (black squares) and at the ROI called Wall 2 (red circles). Despite the lower temporal resolution, we can see how the intensity at Wall 2 also follows closely the strong oscillations at the divertor. Although not strictly necessarily, the emission there could have a strong contribution of stray light from the divertor. Contrarily, the emission at the OMP limiter corresponding to our observation region along this study, stays constant within $\pm 10\%$. It shows no time correlation with the strongly oscillating divertor light and therefore it can be concluded that the contribution of reflections should be small.

Summarizing, the D_α emission at the limiters OMP observation region is not dominated by divertor reflections for the here analysed plasmas. However, they might contribute to some extent to the total measurement. If in the future, if the effect of the reflected light can be quantified, the here presented results can be easily corrected by subtracting its contribution in the following simple way. Defining the total measured D_α radiance $L^*{}_{D\alpha}$, as the sum of the radiance coming from the emission volume at the limiter $L_{D\alpha}$ (the quantity to be measured) and the one due to reflections at its surface $L^R{}_{D\alpha}$, we have:

$$L_{D\alpha} = L^*_{D_\alpha} - L^{Ref}_{D_\alpha} = L^*_{D_\alpha}(1-r), \quad (6)$$

where $r = L^R{}_{D\alpha}/L^*{}_{D\alpha}$ is the fraction of surface reflected light. Correspondingly, to get the real yield Y^{eff} as defined in equation (3) from the apparent measured effective sputtering $Y^{eff\,*}$ that includes D_α light reflections, we get:

$$Y^{eff} = Y^{eff\,*}(1-r)^{-1}. \quad (7)$$

As an example, if $r = 0.2$, then the effective sputtering yield Y^{eff} corrected for reflections would be a factor of 1.25 higher than the one estimated with the total measured D_α radiance.

ORCID iDs

E. de la Cal https://orcid.org/0000-0001-8020-7682
E.R. Solano https://orcid.org/0000-0002-4815-3407
I. Balboa https://orcid.org/0000-0002-5665-2222
S. Silburn https://orcid.org/0000-0002-3111-5113
E. Pawelec https://orcid.org/0000-0003-1333-6331
J. Romazanov https://orcid.org/0000-0001-9439-786X
R. Chapman https://orcid.org/0000-0002-3842-1420
A. Gonzalez https://orcid.org/0000-0002-7217-7310
L. Xiang https://orcid.org/0000-0001-8175-6640

References

[1] Pitcher C.S. and Stangeby P. 1997 *Plasma Phys. Control. Fusion* **39** 779
[2] Lipschultz B. *et al* 2007 *Nucl. Fusion* **47** 1189
[3] Labombard B. *et al* 1997 *J. Nucl. Mater.* **241** 149
[4] Rudakov D. *et al* 2005 *Nucl. Fusion* **45** 1589
[5] Whyte D., Lipschultz B.L., Stangeby P.C., Boedo J., Rudakov D.L., Watkins J.G. and West W.P. 2005 *Plasma Phys. Control. Fusion* **47** 1579
[6] Romazanov J. *et al* 2022 *Nucl. Fusion* **62** 036011
[7] Schmid K. 2022 *Nucl. Mater. Energy* **33** 101230
[8] Maggi C.F. *et al* 2024 *Nucl. Fusion* **64** 112012
[9] Borodkina I. *et al* 2024 *Nucl. Fusion* **64** 106009
[10] Douai D. *et al*, *29th IAEA Fusion Energy Conf. (FEC 2023)* (*London, United Kingdom, 16–21 October 2023*) (available at: https://www.iaea.org/events/fec2023)
[11] Stamp M., Krieger K. and Brezinsek S. 2010 *J. Nucl. Mater.* **415** S170
[12] Brezinsek S., Stamp M.F., Nishijima D., Borodin D., Devaux S., Krieger K., Marsen S., O'Mullane M., Bjoerkas C. and Kirschner A. 2014 *Nucl. Fusion* **54** 103001
[13] Brezinsek S. *et al* 2015 *Nucl. Fusion* **55** 063021
[14] Borodin D. *et al* 2014 *Phys. Scr.* **159** 014057
[15] De Temmerman G. *et al* 2021 *Nucl. Mater. Energy* **27** 100994
[16] de la Cal E. *et al* 2022 *Nucl. Fusion* **62** 126001
[17] de la Cal E. *et al* 2022 *Nucl. Fusion* **62** 126021
[18] Mutzke A. *et al* 2019 SDTrim SP version 6.00 *Report IPP 2019–02 Technical Report*
[19] Balboa I. *et al* 2023 *Plasma Phys. Control. Fusion* **65** 064005
[20] de la Cal E. *et al* 2020 *Plasma Phys. Control. Fusion* **62** 035006
[21] Losada U., Manzanares A., Balboa I., Silburn S., Karhunen J., Carvalho P.J., Huber A., Huber V., Solano E.R. and de la Cal E. 2020 *Nucl. Mater. Energy* **25** 100837
[22] Huber V. *et al* 2019 *Nucl. Fusion* **59** 076016
[23] Maggi C.F. *et al* 2018 *Plasma Phys. Control. Fusion* **60** 014045
[24] Solano E.R. *et al* 2022 *Nucl. Fusion* **62** 076026
[25] Birkenmeier G. *et al* 2023 *Plasma Phys. Control. Fusion* **65** 054001
[26] Behringer K.H., Summers H.P., Denne B., Forrest M. and Stamp M. 1989 *Plasma Phys. Control. Fusion* **31** 2059
[27] Summers H.P. ADAS (available at: http://www.adas.ac.uk)
[28] Mertens P., Brezinsek S., Greenland P.T., Hey J.D., Pospieszczyk A., Reiter D., Samm U., Schweer B., Sergienko G. and Vietzke E. 2001 *Plasma Phys. Control. Fusion* **43** A349
[29] Brezinsek S., Sergienko G., Pospieszczyk A., Mertens P., Samm U. and Greenland P.T. 2005 *Plasma Phys. Control. Fusion* **47** 615
[30] de la Cal E. *et al* 2008 *Nucl. Fusion* **48** 095005
[31] Kremeyer T. *et al* 2022 *Nucl. Fusion* **62** 036023
[32] JET Team 1989 *J. Nucl. Mater.* **162–164** 3
[33] Tagle J.A., Clement S., Loarte A., de Kock L., Harbour P.J., O'Brien D., Erents S.K., Janeschitz G., Nicholson C. and Vince J. 1992 *J. Nucl. Mater.* **196–198** 409
[34] Groth M. *et al* 2013 *Nucl. Fusion* **53** 093016
[35] Wynn A. *et al* 2018 *Nucl. Fusion* **58** 056001
[36] Scarabosio A., Eich T., Herrmann A. and Sieglin B. 2013 *J. Nucl. Mater.* **438** S426
[37] Colas L. *et al* 2022 *Nucl. Fusion* **62** 016014
[38] Roth J., Eckstein W. and Guseva M. 1997 *Fusion Eng. Des.* **37** 465
[39] Babenko P.Y., Mironov M.I., Mikhailov V.S. and Zinoviev A.N. 2020 *Plasma Phys. Control. Fusion* **62** 045020
[40] Borodin D. *et al* 2021 *2021 47th EPS Conf. on Plasma Physics* (*Sitges, Spain*) p P1.1029 (available at: https://epsplasma2020.eu/)
[41] Nishijima D., Doerner R.P., Baldwin M.J., De Temmerman G. and Hollmann E.M. 2008 *Plasma Phys. Control. Fusion* **50** 125007
[42] Björkas C., Vörtler K., Nordlund K., Nishijima D. and Doerner R. 2009 *New J. Phys.* **11** 123017
[43] Romazanov J. *et al 29th IAEA Fusion Energy Conf. (FEC 2023)* (*London, United Kingdom, 16–21 October 2023*) (available at: https://www.iaea.org/events/fec2023)
[44] Clement S., Tagle J.A., Erents S.K., De Kock L., Sartori R. and Saibene G. 1990 *J. Nucl. Mater.* **176–177** 432
[45] Carr M. *et al* 2019 *Rev. Sci. Instrum.* **90** 043504
[46] Karhunen J. *et al* 2019 *Rev. Sci. Instrum.* **90** 103504
[47] Neverov V.S. *et al* 2024 *Plasma Phys. Control. Fusion* **66** 025010